Hybrid Rocket Motors Regression Rate Prediction through CFD Simulations

Martina Faenza, Francesco Barato**, Marta Lazzarin** and Daniele Pavarin***

**Nammo Raufoss AS, Enggata 37, 2831 Raufoss, Norway*

*** Department of Industrial Engineering, Center of Studies and Activities for Space G. Colombo, University of Padua, Via Venezia 59/4, Padova, Italy, 35131*

Abstract

The regression rate is a fundamental parameter determining hybrid rocket motor performances. Unfortunately, hybrid regression rate varies with time, space and scale and it is very difficult to predict because is dependent on the complex interaction between different wide-ranging physical phenomena. Computational fluid dynamics (CFD) represents a useful tool both to predict motor behavior, supporting design phases, and to investigate the internal ballistic of the motor, contributing to physical understanding. University of Padua has implemented on a commercial CFD code a specific user-defined function that calculates regression rate, cell by cell, as a function of heat flux at the fuel surface. The regression rate is determined solving the energy balance at the surface coupled with the Arrhenius equation for fuel pyrolysis. A validation campaign has been successfully performed referring to literature data from Carmicino and Sorge. The numerical determined fuel mass flows generally agree within 10% with the experimental results. The numerical tool can thus be used to perform parametric analysis in order to investigate hybrid rocket motor regression rate behavior.

Nomenclature

A	*surface*	Y	*mass fraction*
A_a	*Arrhenius pre-exponential factor*	x_{max}	*axial location of maximum regression rate*
c	*specific heat capacity*	z	*direction normal to the surface*
c^*	*characteristic velocity*	R_u	*universal gas constant*
D	*mass diffusivity*	$\dot{m}$	*mass flow rate*
D_{p0}	*fuel grain initial port diameter*	ΔH^0	*enthalpy of formation*
D_{pm}	*fuel grain mean port diameter*	κ	*thermal conductivity*
E_c	*energy of activation*	ρ	*density*
G	*mass flux*	*Subscripts*	
GOX	*gaseous oxygen*	f	*fuel (solid phase)*
HDPE	*high density polyethylene*	g	*gas phase*
HTPB	*hydroxyl-terminated polybutadiene*	i	*i-species*
L_g	*fuel grain length*	ox	*oxidizer*
OF	*oxidizer to fuel ratio*	rad	*radiation*
p	*pressure*	ref	*reference condition*
Q	*heat flux*	s	*condition at the surface*
t_b	*burning time*	0	*initial condition, condition at* ∞
T	*temperature*	$+$	*above the fuel surface (gas phase side)*
v	*velocity*	$-$	*below the fuel surface (solid phase side)*

1. Introduction

Hybrid rockets have several potential advantages like simplicity, low cost, safety, reliability and environmental friendliness, together with thrust modulation and restart-ability. However, hybrid rocket propulsion has still to reach a sufficient maturity to achieve operational status. In this perspective, computational fluid dynamics (CFD) represents a fundamental tool to develop high performing solutions and increasing the TRL of hybrid motors in a cost-effective way. In fact, CFD can be used to perform parametric analysis, to predict motor behavior, and finally to investigate specific local details of the internal ballistic, compensating the lack of information provided by experiments, which usually can give

just global information mainly about pressure, flow rates and thrust. All these aspects allow to reduce the number of required tests and to drive efficiently development programs avoiding the expensive trial-and-error practice.

In particular, hybrid regression rate is a very difficult parameter to predict because it varies with time, position and scale. It represents a significant unknown variable in the motor operation until the motor is tested: data are usually available from literature, but not often totally extendible to the specific case, as regression rate depends both on chemical and physical properties of the selected propellants, as well as on geometrical and fluid-dynamics characteristics of the motor (i.e. internal geometry and type of injection).

Several previous attempts have been done in order to predict hybrid regression rate through CFD simulations. Merkle and Venkateswaran[1] developed a comprehensive model that was comprised of the complete time-dependent Navier-Stokes equations, coupled to auxiliary transport equations and physical submodels. The model included the effects of finite rate chemistry, turbulence, gas-phase radiation and coupling of the gas-phase to the solid (fuel) phase. In 2001, Akyuzlu et al.[2] published a paper about a mathematical model predicting regression rate in an ablating hybrid rocket solid fuel. Serin and Gogus[3] have carried out investigations on CFD simulations of hybrid rockets in 2003. They studied the HTPB/O2 reacting flow field of hybrid rocket motors and the corresponding regression rate. They used a commercial Navier-Stokes code, CFD-ACE, to understand the mechanisms affecting regression rate. The regression rate for steady-state conditions was computed by an interactive solution with the program REGRESS. In 2005, Antoniou and Akyuzlu[4] published a mathematical model predicting the entire hybrid rocket motor performance. Guobiao and Hui wrote a paper[5] about their theoretical analysis of propellant performance, solid fuel regression rate and characteristic of combustion and flow in hybrid rockets. They studied also fuel regression rate and combustion flow on a computational point of view. Recently, Bianchi et al.[6] performed numerical simulations of the flow in a GOX/HTPB hybrid rocket engine with a Reynolds averaged Navier-Stokes solver including detailed gas surface interaction modeling based on mass and energy balances. Moreover, fuel pyrolysis and heterogeneous reactions at the nozzle wall were included via finite-rate Arrhenius kinetics. In the framework of the SPARTAN[7] program, University of Padua (UPD) was responsible of customizing a CFD software to accurately simulate hybrid motor operations, thus supporting design and testing phases[8]. The CFD tool selected by UPD for these scopes is a commercial code; this choice reduces development costs but gives the possibility to tailor the setup on specific needs related to the hybrid rocket combustion. A forward step for UPD in the numerical modeling of hybrid combustion consisted in self-evaluating fuel regression rate as a function of wall heat flux.

The self-calculation of regression rate has been obtained thanks to the implementation of a specific User-Defined Function (UDF): a function programmed by the user in C language, which can be dynamically coupled with the CFD solver to enhance the standard features of the commercial code.

In the following sections a description of both the theoretical and numerical model adopted will be provided. Then the numerical results will be presented in comparison with the reference experimental data and the most interesting aspects of the flow field will be discussed.

2. Theoretical Model

In order to predict the fuel regression rate in hybrid rocket motors, the gaseous-solid interface has to be resolved. Because of the heat flux provided to the solid surface by the combustion process itself, new pyrolyzed and gasified fuel mass flow rate is released in the chamber to interact with the incoming oxidizer, in a self-sustained mechanism.

A turbulent diffusion flame is established within the boundary layer as a result of coupling of different processes:

- kinetics of the condensed phase pyrolysis;
- homogenous combustion mechanism in gaseous phase;
- convective and radiative heat transfer in gaseous phase;
- mass transfer of the chemical species.

Kuo [9] and Chiaverini [10] well showed the contribution of these mechanisms in defining the net heat flux through the pyrolyzing surface in the schematic representation reported in Figure 1.

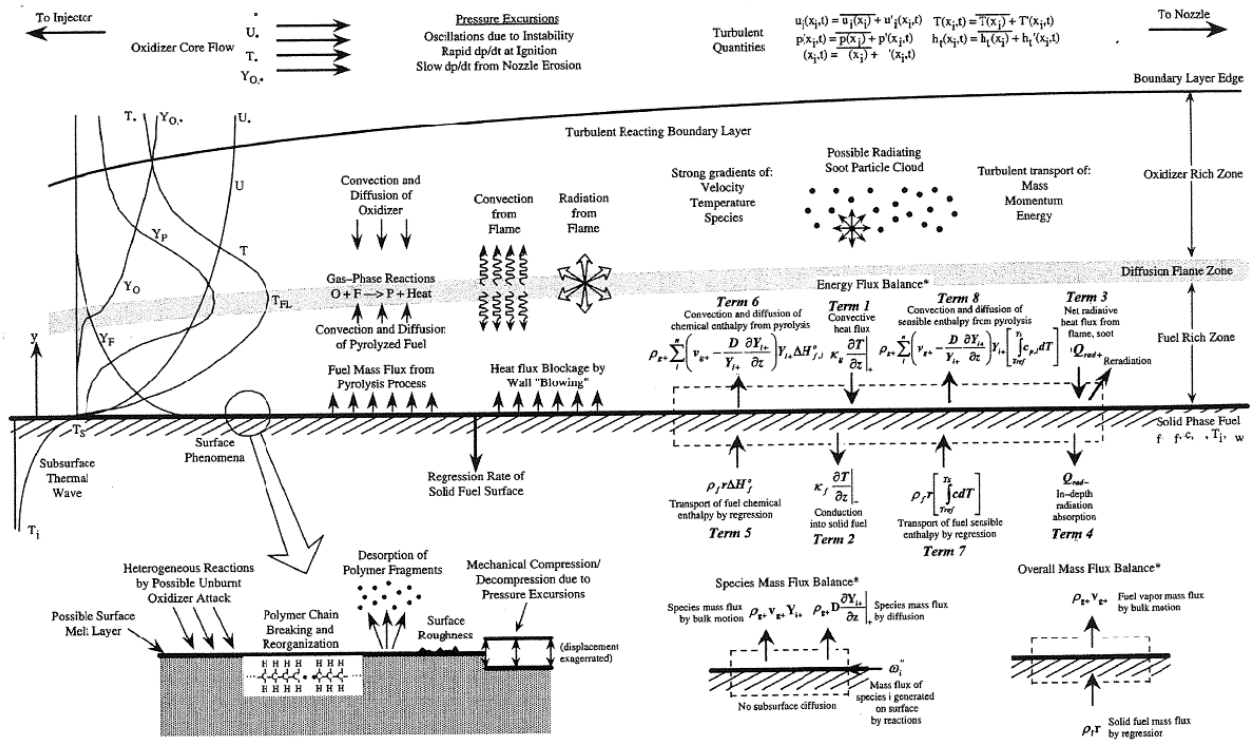

Figure 1: Physical processes involved in hybrid rocket combustion[9]

According to this scheme, a control volume can be located at the very interface between gas and solid and the conservation of mass and energy can be balanced through the volume.

Based on the scheme of Figure 1, the overall mass flux balance can be expressed as:

$$\frac{\dot{m}}{A} = \rho_g v_{g+} = \rho_f \dot{r} \tag{1}$$

While the energy flux balance for a surface fixed in space can be written as:

$$\underbrace{\rho_f \dot{r}\left(\Delta H_f^o + \int_{T_{ref}}^{T} c_f dT\right) - \kappa_g \left.\frac{\partial T}{\partial z}\right|_+ + Q_{rad+}}_{absorbed\ by\ the\ surface} = \underbrace{\rho_{g+} \sum_i^n v_{g+} Y_{i+}\left(\Delta H_{g,i}^o + \int_{T_{ref}}^{T} c_{g,i} dT\right) - \rho_{g+} \sum_i^n D \frac{\partial Y_{i+}}{\partial z}\left(\Delta H_{g,i}^o + \int_{T_{ref}}^{T} c_{g,i} dT\right) - \kappa_f \left.\frac{\partial T}{\partial z}\right|_- + Q_{rad-}}_{released\ by\ the\ surface} \tag{2}$$

As stated in the equation, the left side terms represent energy fluxes entering the fuel surface while the ones on the right side the fluxes leaving the surface.

The first term on the left side represents the contribution of both chemical and sensible enthalpy due to the ablation of the solid fuel; the second term and third term are heat fed to the surface by combustion to sustain the regression process by convection and radiation respectively. The first and second term on the right side account for both chemical and sensible enthalpy of the *n* pyrolysis products leaving the surface both through bulk flow and diffusion; the identity and mass fraction of the products of pyrolysis must then be known. Finally the last two terms correspond to heat fluxes released by conduction and radiation towards the solid subsurface.

The thermal energy leaving the surface because of conduction through the fuel grain can be computed applying the energy equation for the solid phase in the z (normal) direction, assuming negligible any variation of fuel thermal conductivity, κ_f, and specific heat capacity, c_f, as a function of temperature. Combining the energy equation with (1):

$$\kappa_f \frac{d^2T}{d^2z} - \rho_f \dot{r} c_f \frac{dT}{dz} = 0 \tag{3}$$

Equation (3) has a general solution of the form:

$$T(z) = C_1 + C_2 \exp\left[\left(\rho_f c_f / \kappa_f\right)\dot{r} z\right] \tag{4}$$

Where C_1 and C_2 coefficients can be determined considering $T(z=0) = T_s$ and $T(z=-) = T_0$as boundary conditions, to get to:

$$T(z) = T_0 + (T_s - T_0)\exp\left[\left(\rho_f c_f / \kappa_f\right)\dot{r} z\right] \tag{5}$$

Therefore the temperature profile within the fuel grain varies exponentially as a function of depth *z*. Taking the first derivative of equation (5) at the fuel surface ($z = 0$), the following equivalence is obtained:

$$\kappa_f \left.\frac{dT}{dz}\right|_{z=0} = \rho_f c_f \dot{r}(T_s - T_0) \tag{6}$$

This expression of subsurface heat conduction can be combined with equation (2). A further simplification of equation (2) can be made considering the term Q_{rad-}: typically the radiation through the subsurface of the fuel grain can be considered negligible either because most of the fuel are opaque by themselves to thermal radiation or because they are made so by adding a small percentage of carbon powder to the mixture during the manufacturing process.

Furthermore, considering an average value of c_f as a function of temperature, as for equation (3), the chemical and sensible contribution of fuel ablation in equation (2) can be rewritten as:

$$\int_{T_{ref}}^{T} c_f dT = c_f\left(T_s - T_{ref}\right) \tag{7}$$

Finally, the velocity due to diffusion of the pyrolyzed species can be considered negligible respect to the bulk velocity, thus:

$$\frac{\partial Y_{i+}}{\partial z} \approx 0 \tag{8}$$

Equation (2) can now be reformulated combining equation (1), equation (6), $Q_{rad-} \approx 0$, equation (7), and equation (8) to get to:

$$-\kappa_g \left.\frac{\partial T}{\partial z}\right|_{+} + Q_{rad+} = -\rho_f \dot{r}\left[\Delta H_f^o + c_f\left(T_s - T_{ref}\right)\right] + \rho_f \dot{r} \sum_i^n Y_{i+}\left[\Delta H_{g,i}^o + \int_{T_{ref}}^{T_s} c_{g,i} dT\right] + + \rho_f c_f \dot{r}(T_s - T_0) \tag{9}$$

Usually the initial temperature of the fuel grain, and thus the temperature that the fuel grain maintains at the $z = -$ boundary is the ambient one, thus 298 K, which can then be adopted as the reference value to calculate the sensible enthalpy, being that the standard enthalpy of formation is given in literature at the same temperature. If then $T_0 = T_{ref} = 298\ K$, the energy leaving the surface because of conduction towards the subsurface counteract equally the sensible enthalpy contribution delivered to the surface by the ablation process; equation (9) then simplifies further and becomes:

$$-\kappa_g \left.\frac{\partial T}{\partial z}\right|_{+} + Q_{rad+} = \rho_f \dot{r}\left[\sum_i^n Y_{i+}\left(\Delta H_{g,i}^o + \int_{T_0}^{T_s} c_{g,i} dT\right) - \Delta H_f^o\right] \tag{10}$$

Equation (10) basically means that the heat flux received by convection and radiation from the combustion process is equal to the net energy required to transform the solid fuel in its pyrolysis products at standard state and then to increase the temperature of the pyrolysis product to the actual surface temperature.

In the present study, equation (10) is further simplified, neglecting the contribution of radiation from the combustion process $Q_{rad+} \approx 0$, and simplifying the pyrolysis process so that the solid fuel polymer decomposes directly into its unique gaseous monomer in one step: thus the number of pyrolysis products is reduced to 1 and equation (10) becomes:

$$-\kappa_g \left.\frac{\partial T}{\partial z}\right|_{+} = \rho_f \dot{r}\left[\Delta H_g^o - \Delta H_f^o + \int_{T_0}^{T_s} c_g dT\right] \tag{11}$$

In equation (11), a polynomial expression for the specific heat capacity of the pyrolysis monomer can be adopted to integrate numerically the sensible contribution.

Kinetics of the pyrolysis process completes the set of equation; a first-order reaction approach is adopted:

$$\dot{r}(T_s) = A_a \exp(-E_c/2R_u T_s) \quad (12)$$

Equations (11) and (12) represent the solving system of equations to be solved iteratively for $\dot{r}$ and T_s. The convection heat flux in equation (11) is provided by the CFD solver.

3. Reference Experimental Data

Experimental data from the University of Naples in Italy have been used as benchmark for validating the numerical model. Carmicino and Sorge have performed lab-scale testing both on GOX-HDPE([14], [15], [16]) and GOX-HTPB ([17], [18]) hybrid rockets. In the wide panorama of hybrids lab-scale testing published in literature, the selection of these specific test cases has been driven by several factors:

- Motor configurations and dimensions are well documented and detailed, so it's possible to reply the corresponding fluid geometries in the CFD model without significant uncertainties;
- Test results are clear and thorough and span different port diameters, mass flow rates and thus oxidizer fluxes;
- Motor geometry is simple and axis-symmetric: single-hole axial injector, single port cylindrical grain; this makes possible to simplify the geometrical representation in a 2D model based on axis-symmetry within the CFD model, thus reducing the computational effort required;
- Oxidizer is injected in gaseous phase, so there is no need of simulating a multiphase flow to represent the liquid oxidizer evaporation;
- Fuels used are of common use in hybrids, their properties then being well documented in literature; moreover they are not part of the so-called "liquefying fuels" and thus the regression process can be described as a solid-gaseous phase conversion.

Table 1, Table 2, and Table 3 report all the data taken into account to perform the numerical validation. In the following, the prefix "C2009" will be appended to IDs reported in Table 2 and the prefix "OrC" to IDs reported in Table 3 to compare results from GOX-HTPB tests. For full details about motor configuration and experimental results the reader is referred to [14], [15], [16], [17], and [18].

Table 1: experimental data from literature for a lab-scale GOX-HDPE motor ([14], [15], [16])

ID	L_g *[mm]*	D_{p0} *[mm]*	*p [atm]*	m_{ox} *[kg/s]*	t_b *[s]*	G_{ox} *[kg/m²s]*	m_f *[kg/s]*	*G [kg/m²s]*	*OF*	*c* [m/s]*	*eff*	D_{pm} *[mm]*	*r [mm/s]*	x_{max} *[mm]*
1	560	25	15.63	0.136	24.2	99.69	0.04975	136.1	2.74	1712	0.922	41.71	0.69	280
2	560	50	16.85	0.125	54.9	27.68	0.06111	41.21	2.05	1843	0.952	75.84	0.47	320
3	560	16	17.31	0.124	58.3	63.87	0.04971	89.46	2.5	2028	1.075	49.73	0.58	280
4	560	16	15.64	0.129	43	87.14	0.04800	119.46	2.7	1796	0.965	43.48	0.64	-
5	560	16	15.46	0.124	40.3	92.43	0.04501	125.9	2.76	1892	1.021	41.38	0.63	260
6	560	25	25.00	0.208	42.6	84.8	0.07042	113.51	2.95	1814	0.984	55.88	0.72	320
7	560	25	18.96	0.157	50.4	66.6	0.05534	90.12	2.83	1805	0.976	54.73	0.59	-
8	560	50	22.69	0.188	40.6	47.79	0.06365	63.96	2.96	1828	0.994	70.8	0.51	280
9	560	75	22.61	0.18	31.5	28.41	0.07213	39.79	2.5	1820	0.962	89.84	0.47	400
10	560	25	20.25	0.177	21.2	126	0.05863	167.67	3.02	1748	0.955	42.33	0.82	320
11	560	50	20.78	0.173	33.1	47.45	0.06332	64.85	2.73	1793	0.962	68.08	0.55	240
12	560	75	13.80	0.106	15.2	20.31	0.05928	31.71	1.78	1691	0.869	81.37	0.42	320
13	560	50	10.09	0.08	26.2	28.19	0.03889	41.92	2.05	1731	0.900	60.04	0.38	320
14	560	70	15.57	0.118	36.5	20.95	0.05666	31.03	2.08	1816	0.941	84.56	0.4	-
15	560	75	15.12	0.112	22.8	20.12	0.05912	30.69	1.9	1794	0.923	84.37	0.41	380
16	560	75	15.48	0.112	25.1	19.93	0.05606	29.87	2	1872	0.967	84.72	0.39	280
17	560	50	12.20	0.099	24.2	34.13	0.04517	49.75	2.19	1758	0.919	60.68	0.44	240
18	560	16	11.78	0.1	44.1	78.07	0.03771	107.6	2.64	1741	0.936	40.32	0.55	300
19	560	25	11.11	0.095	44.3	54.03	0.03991	76.85	2.37	1683	0.890	47.19	0.5	none
20	560	54	11.96	0.097	50	23	0.04670	24.27	2.06	1702	0.884	73.04	0.38	260
21	560	50	9.57	0.076	61.5	18.77	0.04311	29.46	1.76	1641	0.846	71.67	0.35	200

Table 2: experimental data from literature for a lab-scale GOX-HTPB motor ([17])

ID	*Lg [mm]*	*Dp0 [mm]*	*tb [s]*	*mox [kg/s]*	*pc1 [bar]*	*pc2 [bar]*	*c* [m/s]*	*eff*	*Dpm [mm]*	*L/D*	*Dpf/Dp0*	*r [mm/s]*	*OF*	*Gox [kg/m2s]*
1	572	25	27.9	0.032	4.6	4.5	1393	0.934	38.84	14.73	2.11	0.496	0.969	27
2	574	25	18.7	0.1328	16.4	16.2	1615	0.894	42.43	13.53	2.39	0.931	1.942	94
3	572	25	12	0.1924	23.7	23.5	1632	0.906	41.15	13.9	2.29	1.343	2.058	145
10bis	572	75	19.6	0.0697	10.2	10.0	1540	0.965	83.31	6.87	1.22	0.419	1.153	13
10	570	50	13.8	0.0468	7.0	6.8	1480	0.976	56.62	10.05	1.26	0.473	1.01	19
11	570	50	8	0.1886	23.9	23.7	1661	0.917	57.70	9.88	1.3	0.954	1.994	72
12	572	50	8.2	0.1966	24.7	24.6	1689	0.933	57.91	9.88	1.32	0.961	2.056	75

Table 3: experimental data from literature for a lab-scale GOX-HTPB motor ([18])

ID	*Lg [mm]*	*Dp0 [mm]*	*mox [kg/s]*	*Gox [kg/m2s]*	*OF*	*mf [kg/s]*	*G [kg/m2s]*	*pc1 [bar]*	*pc2 [bar]*	*r [mm/s]*	*Dpm [mm]*	*c* [m/s]*	*eff*
1	570	20	0.0256	40	0.948	0.0270	81.5	3.92	3.78	0.556	27.92	1481	0.972
2	570	20	0.0718	55	1.576	0.0456	89.8	10.29	10.18	0.659	40.03	1771	0.984
3	570	20	0.1367	60	1.897	0.0721	91.3	18.82	18.76	0.773	50.15	1805	1.01
4	570	20	0.0869	129	1.892	0.0459	197	11.45	11.08	0.923	28.54	1778	0.944
5	570	20	0.1442	145	2.094	0.0689	214.8	17.95	17.85	1.134	33.03	1773	0.95
7	570	20	0.115	211	2.126	0.0541	309.7	14.62	13.96	1.19	25.6	1764	0.941
8	570	20	0.1848	219	2.345	0.0788	312.5	22.92	22.48	1.393	30.46	1755	0.977

Referring to the experimental results just reported, it has to be highlighted that, due to the peculiar coupling between oxidizer flow pattern at injection and motor internal geometry, the resulting average regression rate is strongly correlated with the port diameter history that leaded to its value ([16] and [18]): thus in order to make a proper comparison between experimental and numerical results, not just the correspondence of oxidizer mass flux but also of average port diameter is taken into account.

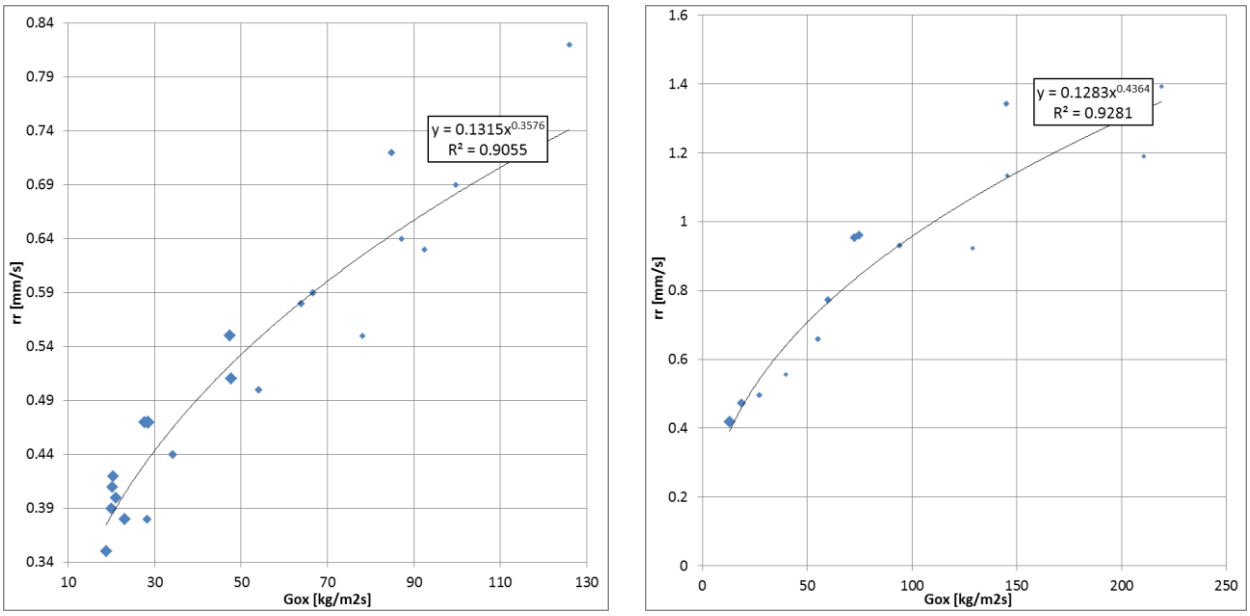

Figure 2: regression rate as a function of oxidizer flux for the GOX-HDPE motor (left, data in Table 1) and the GOX-HTPB one (right, Table 2 and Table 3); different average port diameter corresponding to each point is represented by the dimension of the symbols

Figure 2 shows the plots of regression rate as a function of oxidizer mass flux for the reported data, highlighting the different average port diameters which they correspond to.

4. Fuel Characteristics

In order to solve the system of equations composed by eq. (11) and eq. (12) several physical parameters regarding the solid fuel and its constituent monomer are needed.

"C2H4" and "C4H6 1,3 butadiene" are considered to be the major constituent monomers for HDPE and HTPB respectively, based on the typical conditions of heat flux and fuel surface temperature expected in the hybrid motor ([10] and [13]).

The physical characteristics needed to implement the model are then:

- Solid fuel density, ρ_f;
- Enthalpy of formation of fuel monomer, ΔH_g^o;
- Enthalpy of formation of solid fuel, ΔH_f^o;
- Specific heat capacity of fuel monomer, c_g;
- Arrhenius pre-exponential factor, A_a;
- Energy of activation, E_c.

Many sources can be found in literature reporting all these data and most of the time there is a limited scattering of values. In general there is satisfying coherence about all the listed data for HDPE, while data for HTPB denote quite a huge scattering and disagreement among the sources, especially for what concerns the parameters of the Arrhenius equation and the enthalpy of formation of the solid fuel ([13], [19], [20], [21], [22], [23], [24]). This discrepancy can be explained both by the large variety of methods which the estimation of the parameters is based on ([10] and [13]) and by the wide range of slightly different compositions that falls within the same tag of HTPB.

NASA-Glenn and NIST databases have been adopted as a reference for HTPB thermochemical properties since they represent consolidate and reliable references, while for the parameters in the Arrhenius equation, data published by Chiaverini ([10]) have been considered.

As far as Arrhenius parameters for HDPE are concerned, the approach of Lengellé has been adopted to estimate the pre-exponential factor, that in this context we indicate as $\bar{A}_a$ ([12], [13]):

$$\bar{A}_a = \sqrt{\frac{A_c d_p R_u}{E_c}} \sqrt{\bar{T}_s} \sqrt{1 \Big/ \left[-\ln\left(Y_{p,s}\right)\left(1 - \frac{T_0}{T_s} + \frac{h_d}{\bar{c}_p T_s}\right) - \frac{h_D}{\bar{c}_p T_s} \right]} \tag{13}$$

In eq. (13), $\bar{T}_s$ is the mean fuel surface temperature, A_c is the Arrhenius pre-exponential factor in [1/s], $\bar{d}_p$ is the mean thermal diffusivity in the temperature range of interest, h_D is the heat of degradation, that is the heat required to convert the solid fuel into its gaseous monomer at T_s, and $\bar{c}_p$ is the mean specific heat capacity in the temperature range of interest. Finally, $Y_{p,s}$ represents the mass fraction of the remaining polymer after fuel degradation in its constituent monomer and can be assumed as a small quantity, 0.01, at the end of the degradation process.

The thermal diffusivity, $\bar{d}_p$, is evaluated as: $\bar{d}_p = \frac{\lambda}{\rho_f \bar{c}_p}$ (14)

Table 4: physical parameters used in the Arrhenius equation for HDPE ([13], [14], [27], [28])

A_c [1/s]	E_c [J/mol]	λ [J/msK]	ρ_f [kg/m3]	$\bar{c}_p$ [J/kgK]	$\bar{d}_p$ [m2/s]	h_D [J/kg]	$Y_{p,s}$	$\bar{T}_s$ [K]	T0 [K]	$\bar{A}_a$ [m/s]
2E+16	251208	0.38	968	1597	2.45812E-07	3190000	0.01	900	300	3636

Table 5: physical parameters used in the Arrhenius equation for HTPB ([10])

	A_a [m/s]	$E_a = E_c/2$ [J/mol]
$T_s < 722\ K$	3.9648	55893.78
$T_s > 722\ K$	0.01104	20557.188

Table 6: enthalpies of formation ([23], [25], [29])

HDPE		*HTPB*	
ΔH_g^o (C2H4) [J/kg]	ΔH_f^o (HDPE) [J/kg]	ΔH_g^o (C4H6 1,3 butadiene) [J/kg]	ΔH_f^o (HTPB) [J/kg]
1871447	-1895352	2033631	-310000

Tables Table 4, Table 5 and Table 6 summarize all the physical parameters aforementioned.

The density considered for HTPB is: $\rho_f = 953$ kg/m3.

Both for HTPB and HDPE, the specific heat capacity for the gaseous monomer, c_g, is calculated as a polynomial function of temperature, according to the coefficients reported in [27], that are the same implemented in the CFD software database.

5. Numerical Model

5.1. User Defined Function

The self-calculation of regression rate has been made possible thanks to the implementation of a specific user-defined function (UDF): a function programmed by the user in C language that can be dynamically coupled with the CFD solver to enhance the standard features of the commercial code. In general, UDFs can be used for example to define particular boundary conditions, material properties, and source terms for the specific flow regime, as well as to specify customized model parameters, initialize a solution, or enhance post-processing.

At each iteration in running the CFD simulation, UDF is called: based on the convective heat flux provided cell by cell at the gaseous interface, the system formed by eq. (11) and (12) is solved to get the new fuel mass flux and fuel surface temperature to be set as boundary conditions for the next iteration (Figure 3).

Within the main *i* iteration of the CFD solver

loop1
- Select faces *f* of Fuel surface *S*
- **for** *f* in *S* **do**
  - $T_s = T(f)$;
  - $Q_{conv} = -\kappa_g \frac{\partial T}{\partial z}\Big|_+$;
  - **loop2, j =1**
    - calculate $H_v(T_s) = \Delta H_g^o - \Delta H_f^o + \int_{T_0}^{T_s} c_g dT$
    - calculate $\dot{r}$ eq. (11)
    - calculate T_s^{new} eq. (12)
  - **loop2, j >1**
    - **repeat**
      - $T_s^{old} = T_s^{new}(j-1)$
      - calculate $H_v(T_s^{old})$
      - calculate $\dot{r}(Q_{conv}, H_v(T_s^{old}))$ eq. (11)
      - calculate T_s^{new} eq. (12)
      - $error = T_s^{new} - T_s^{old}$
      - j++
    - **until** $error < tol$
  - **end loop2**
  - $T_s^{new\prime} = T_s + \alpha(T_s^{new} - T_s)$
  - $T(f) = T_s^{new\prime}$
  - calculate $\dot{r}$ eq. (12)
  - calculate $\dot{G}_f = \rho_f \dot{r}$ eq. (11)
- **end for**

end loop1

Figure 3: pseudo-code representation of the core functioning of UDF to calculate regression rate cell by cell

5.2. Geometry

Figure 4: fluid volume for the CFD simulations. Circle marks represent reference points, which have been used during solving for convergence monitoring on specific parameters

Especially in the case of self-evaluation of regression rate, an extremely refined mesh is required in correspondence of the fuel surface to correctly describe temperature gradients; this need, coupled with a 3D geometry, can cause a serious showstopper, which is the computational effort. In this perspective a 2D geometry is mandatory according to the computational resources available (8 cores processor) to get convergence in a reasonable time (i.e. 8-24 hours). So, in the hypothesis of axis symmetry, a 2D representation of the fluid volume has been adopted imposing an axis symmetry setting to the motor axis.

The main characteristics of the fluid geometry are shown in Figure 4, with the main boundary conditions highlighted. The motor configuration tested at the University of Naples was provided by a calibrated converging venturi as the oxidizer injector; this component has been kept in the fluid geometry representation, in order to let the simulation evaluate the flow characteristics at the motor entrance, based on the development within the venturi. Additionally, the fuel grain front and back sections were protected against burning by means of ablative disks and this aspect has been taken into account in defining the fuel surface inlet, assuming that the diameter of the insulation disk enlarges at the same rate of the fuel grain port diameter.

5.3. Mesh

The mesh is hexahedral and customized to obtain the desired dimension near the walls and a smooth transition between regions with different refinement. Sensitivity studies have been performed in a preliminary phase to identify the final mesh setup. Figure 5 shows a zoomed detail about the resulting mesh. Element thickness at grain surface is equal to 0.001 mm, while on the other walls the thickness is 1 or 2 orders of magnitude higher; the resulting number of cells is in the order of 2÷3e5.

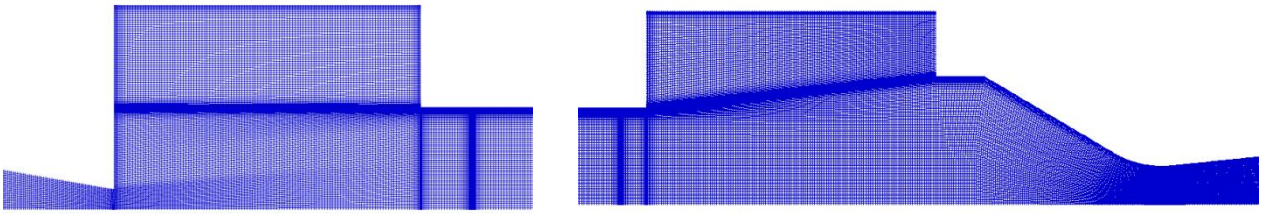

Figure 5: detail of the mesh at the front (left) and back (right) part of the fluid motor

5.4. Combustion Modeling

The Eddy Dissipation model has been selected as the best compromise between accuracy, simplicity, computational effort, reliability and availability of the information required by the setup.

The main assumptions of this model are:

- one forward reaction evaluated at stoichiometric O/F and expected operative pressure by means of CEA software, in hypothesis of chemical equilibrium;
- no re-combinations: this aspect can be relevant where local O/F ratio is substantially different from the stoichiometric value and chemical kinetics becomes not negligible;
- the chemical equilibrium shift as a function of O/F ratio is not considered;
- the reaction rate depends exclusively on turbulent mixing (Damkholer number >>1).

The resulting balance equation set up in the Eddy Dissipation model is reported below, both for O2-C2H4, eq. (15), and O2-C4H6, eq. (16):

$$30\ O_2 + 10\ C_2H_4 \rightarrow 12.2\ CO + 7.8\ CO_2 + 2.1\ H + 2.6\ H_2 + 13.7\ H_2O + 2.6\ O + 5.3\ OH + 5.3\ O_2 \quad (15)$$

$$110\ O_2 + 20\ C_4H_6 \rightarrow 49.6\ CO + 30.4\ CO_2 + 7.7\ H + 7.7\ H_2 + 39.3\ H_2O + 10.6\ O + 18.3\ OH + 20.7\ O_2 \quad (16)$$

It has to be remarked that the Eddy Dissipation model is based on a fixed chemical balance, which does not take into account O/F shifting equilibrium; so for example the pre combustion chamber, where O/F can be considerably different from the nominal/stoichiometric value, can be affected by some inaccuracy in prediction of the correct temperature. Regression rate prediction at the fuel grain, on the contrary, does not suffer from this inaccuracy, since here the O/F ratio is close/equal to the stoichiometric value and the only source of error could come from a not well refined mesh.

5.5. Other settings

Additional relevant settings are listed hereafter.

- The simulation is steady state: the motor functioning at mean port diameter is considered. Each simulation has been run firstly with fixed regression rate and brought to convergence to correctly and accurately initialize the domain; then UDF has been activated. In case of imposed regression rate, its mean from experimental data has been used.
- The fuel grain mean port diameter is assumed constant along the axial direction so the fluid geometry neglects possible unevenness of the regressing fuel surface.
- The k-Ω SST turbulence model has been adopted, excluding wall functions, and the solution has been obtained with double precision and second order upwind discretization scheme.
- Convergence has been tracked both based on residuals and on specific parameters variation (f.i. pressure, temperature, axial velocity) at pre-defined control points in the domain (see Figure 4).
- Concerning the simulations with HTPB as fuel, radiation has not been included in the modeling, since the maturity of modeling radiation for hybrids is such that probably the same amount of uncertainty would be introduced by implementing it in the CFD model. The simulations for HTPB are then performed keeping in mind that a major underestimation of the average regression rate can be found respect to the experimental result, especially at low oxidizer mass fluxes.

6. Results and Discussion

6.1. Comparison with the Experimental Data

Several average port diameters and oxidizer mass fluxes have been span. Pre-defined values of these two parameters have been selected in order to have a good coverage of the records experimentally investigated. Each numerical simulation have been quantitatively compared in terms of regression rate with the corresponding experimental case having the closest values of both port diameter and oxidizer mass flux. In addition, the complete set of numerical results has been compared with the regression rate versus oxidizer mass flux profile obtained experimentally.

Table 7 and Table 8 list the performed simulation with the corresponding settings, and report, where available, the corresponding experimental tests used for direct comparison. The experimental tests are those reported in Table 1, Table 2, and Table 3. Regression rates reported for numerical results have been calculated as the surface weighted average values along the fuel surface.

Table 7: numerical versus experimental results for GOX-HDPE

#	D_{pm} [mm]	G_{ox} [kg/m^{2}s]	m_{ox} [kg/s]	r_{CFD} [mm/s]	Test #	r_{exp} [mm/s]	error
B_L560_D40	40	80	0.1005	0.60	18	0.55	10.0%
A_L560_D40	40	100	0.1257	0.72	1	0.69	4.7%
Q_L560_D40	40	92.43	0.1162	0.68	5	0.63	7.9%
R_L560_D40	40	126	0.1583	0.87	10	0.82	6.1%
H_L560_D50	50	50	0.0982	0.49	-	-	-
G_L560_D50	50	60	0.1178	0.57	3	0.58	-2.0%
S_L560_D50	50	66.6	0.1308	0.62	7	0.59	5.2%
F_L560_D50	50	80	0.1571	0.72	-	-	-

N_L560_D70	70	20	0.0770	0.32	21	0.35	-7.9%
M_L560_D70	70	30	0.1155	0.46	2	0.47	-2.8%
P_L560_D80	80	20	0.1005	0.37	12	0.42	-12.4%

Table 8: numerical versus experimental results for GOX-HTPB

#	D_{pm} [mm]	G_{ox} [kg/m^{2}s]	m_{ox} [kg/s]	r_{CFD} [mm/s]	Test #	r_{exp} [mm/s]	error
D_L570_D30	30	40	0.0283	0.45	OrC, 1	0.56	-20.1%
C_L570_D30	30	129	0.0912	0.93	OrC, 4	0.92	1.3%
B_L570_D30	30	145	0.1025	1.00	OrC, 5	1.13	-11.8%
A_L570_D30	30	220	0.1555	1.25	OrC, 8	1.39	-9.8%
H_L570_D40	40	27	0.0339	0.42	C2009, 1	0.496	-14.8%
G_L570_D40	40	55	0.0691	0.68	OrC, 2	0.66	3.0%
F_L570_D40	40	94	0.1181	0.94	C2009, 2	0.93	1.1%
E_L570_D40	40	145	0.1822	1.18	C2009, 3	1.34	-11.8%
L_L570_D57	57	19	0.0485	0.40	C2009, 10	0.47	-14.3%
I_L570_D57	57	74	0.1888	1.05	C2009, 12	0.96	9.6%
M_L570_D83.3	83.3	13	0.0708	0.40	C2009, 10b	0.42	-4.1%

The maximum error in predicting the average regression rate is limited to a maximum absolute value of 12% for HDPE; the error is due both to over and underestimation. Regarding HTPB a maximum error of 20% has been detected in one case but it is overage around a maximum absolute value of 15%; in most of the cases regression rate is underestimated but there is not a clear trend with respect to oxidizer flux that allows to conclude that this is due to the absence of radiation in the model. It has to be stressed that part of the simulated configurations does not correspond exactly to the experimental configurations which they are compared to: numerical simulations have been performed as said at several pre-defined port diameter and then spanning a range of oxidizer fluxes; then the closest experimental configuration has been chosen for direct comparison. This approach has given the possibility to perform a wide number of simulations in a time-efficient way.

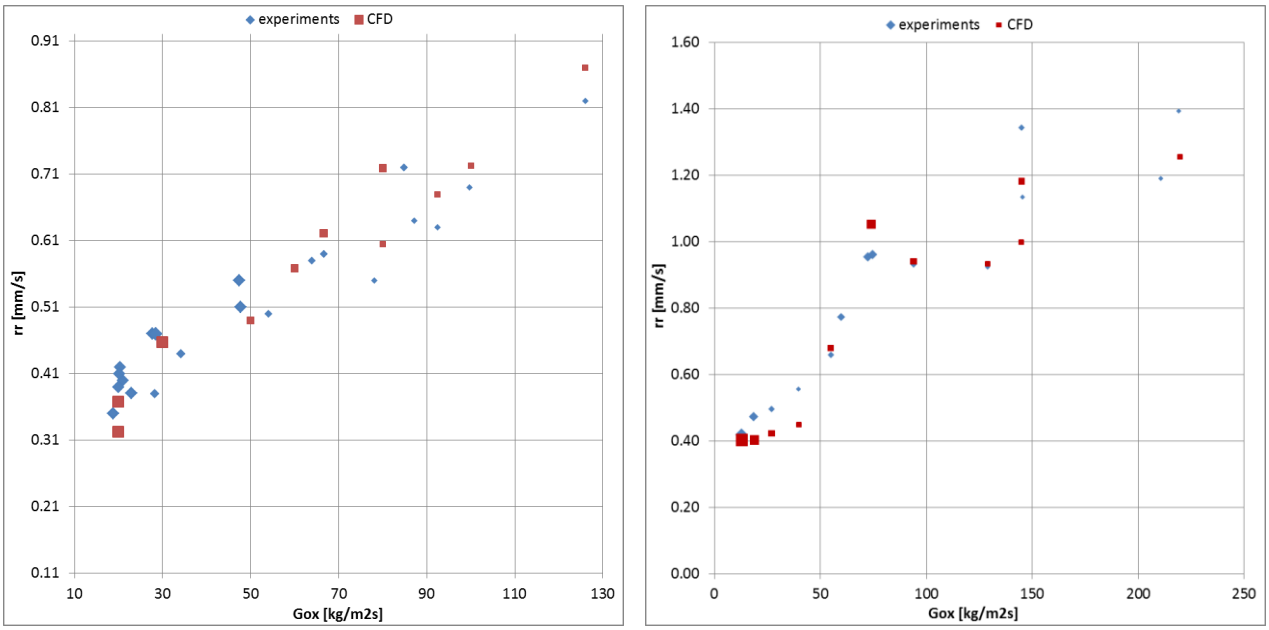

Figure 6: numerical versus experimental regression rate as a function of oxidizer mass flux, for HDPE (left) and HTPB (right)

Figure 6 compares for both HDPE and HTPB cases the regression rate versus oxidizer flux trend obtained by numerical simulations with the one from experiments. It can be clearly seen that both the trend and the absolute values are quite satisfying.

6.2. Comparison with Fixed Regression Rate Simulation

It has been stressed by the authors in a previous paper [31] how the regression rate automatic calculation has a double usefulness respect to the imposing a fixed value: first of all it has a predictive function in providing the global information about the fuel mass flow rate production and secondly it can describe local effects of fuel regression that usually are difficult to be directly observed and studied in experimental tests, like for example impingement. Even though the fixed regression rate model is good in predicting global features of the motor, local variations of heat flux and thus regression rate and thus O/F ratio cannot be analyzed in this case. A comparison between results with fixed regression rate and variable one are considered not relevant in this context. For further insight on this, the reader is referred to [31].

6.3. Parametric Analysis

For the sake of brevity, results showed and discussed in the following are those for HDPE configurations but the very same conclusions apply to HTPB configurations.

In all the following discussion, *x* represents the axial direction, since the fluid volume lies in the *x-y* plane.

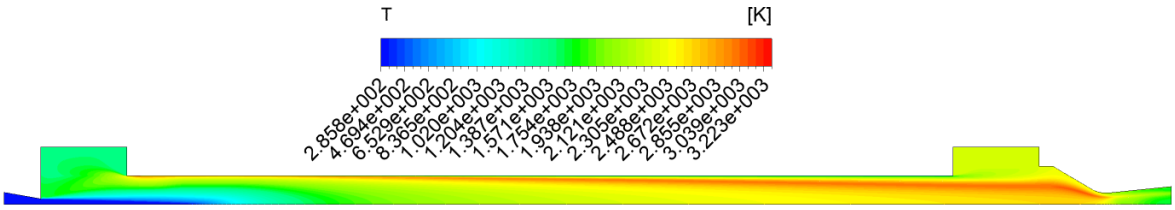

Figure 7: typical temperature contour obtained by hybrid combustion, displaced on an axial plane (simulation *B_L560_D40* of Table 7 is shown)

Figure 7 shows the resulting typical temperature profile inside the combustion chamber: a highly stratified flame is observed, as expected by a single-hole axial injection in hybrids.

Looking at the axial velocity on an axial plane (Figure 8), it can be noticed that there are some areas where backflow settles; apart from the sharp variations of section, where recirculation is expected, this phenomenon is observed also in correspondence of the impingement zone, that is the axial location where the oxidizer literally hit the fuel surface, thus inducing backflow recirculation upstream that point, as shown in Figure 9.

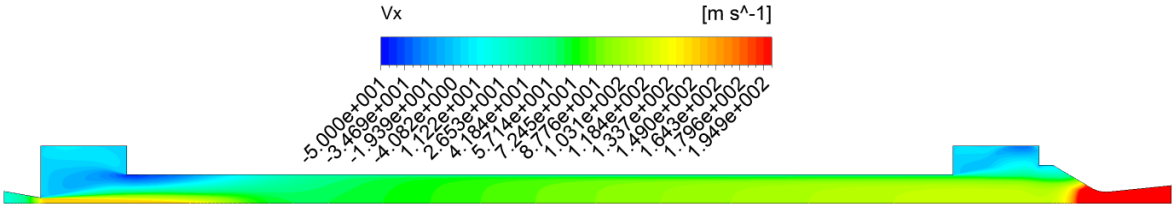

Figure 8: typical axial velocity contour obtained by hybrid combustion, displaced on an axial plane with a limited range to exclude nozzle expansion effect (simulation *B_L560_D40* of Table 7 is shown)

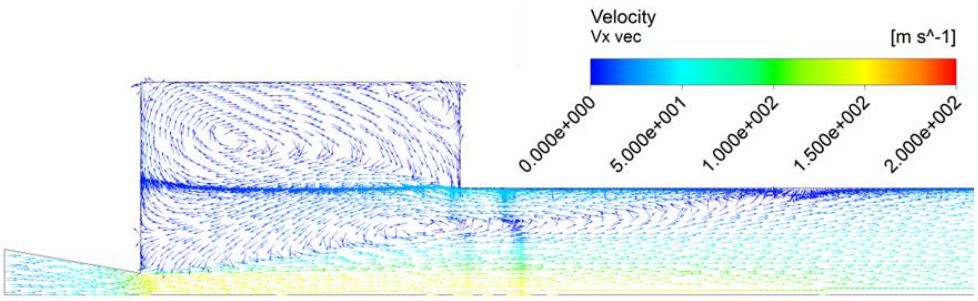

Figure 9: velocity vectors, displaced on an axial plane (simulation *B_L560_D40* of Table 7 is shown)

The backflow causes some combustion products to be dragged towards the pre-combustion chamber. The higher is the turbulent mixing and the closer the local O/F ratio to stoichiometric in this area, the hotter

results the flowfield in this recirculation zone. So for example it has been observed that larger port diameters ease a higher migration and then a locally hotter flowfield. Figure 10 shows what stated: it reports the temperature contour for case *F*, which is characterized by the same oxidizer flux as case *B*, represented in Figure 8, but it has a bigger port diameter; it can be clearly seen that case *F* shows a wider and hotter area upstream the impingement position. It has anyhow to be stressed that the levels of temperature in the pre-combustion chamber are majorly affected by the simplifications introduced by the use of an Eddy Dissipation model of combustion.

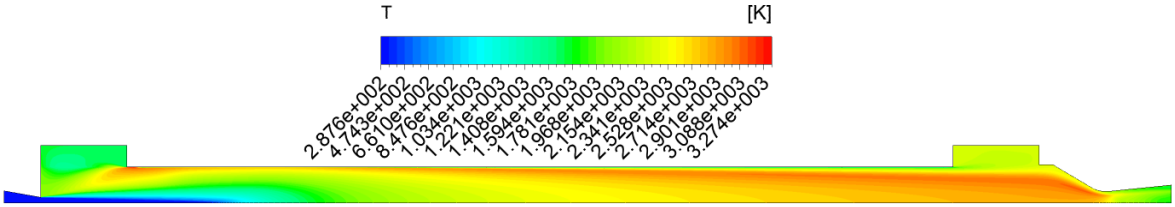

Figure 10: temperature contour displaced on an axial plane for simulation *F_L560_D50* of Table 7

The position of impingement, and thus the resulting flowfield, is strongly influenced by the port diameter which basically sets the distance from the oxidizer inlet to the "impact" surface. Regression rate in correspondence of the impingement position is the highest. Looking then at the regression rate profile along the fuel surface, it can be observed how the position of impingement moves as a function of to the corresponding motor configuration. Figure 11 shows two charts of regression rates profiles corresponding to two different mass flow rates (0.10 kg/s and 0.16 kg/s respectively); each chart reports curves corresponding to cases listed in Table 7 and having the same mass flow rate but different (D_{pm}, G_{ox}) couples. Each chart can then be read as describing how the regression rate profile and the impingement location change during the burning because of port enlarging.

As expected, regression rate peak level decreases with decreasing of the oxidizer flux, and impingement location moves inward the port grain.

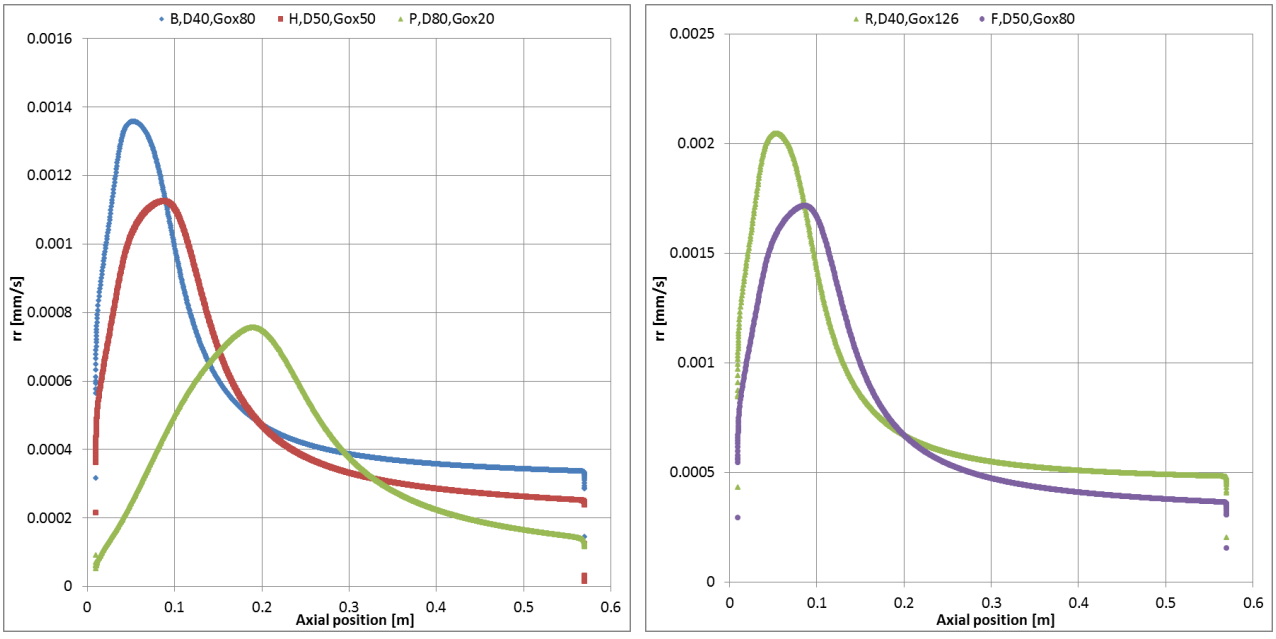

Figure 11: regression rate as a function of axial position along the fuel surface for two different mass flow rates, 0.10 kg/s (left) and 0.16 kg/s (right)

Considering a fixed port diameter then, impingement location is not sensibly affected by the level of oxidizer mass flux while clearly the corresponding regression rate absolute value is so. In Figure 12, two charts for two different fixed diameters (50 mm and 70 mm respectively) and parametric on oxidizer mass flux show was just discussed. At lower oxidizer mass fluxes, the regression rate profile tends to flatten and be more evenly distributed.

Having the same oxidizer flux, larger diameter configurations benefit from a higher regression rate on average (compare f.i. case *H*, Figure 12 (left), with case *L*, Figure 12 (right)) and this could be certainly attributed to the strong impingement effect due to the small size of the injection hole.

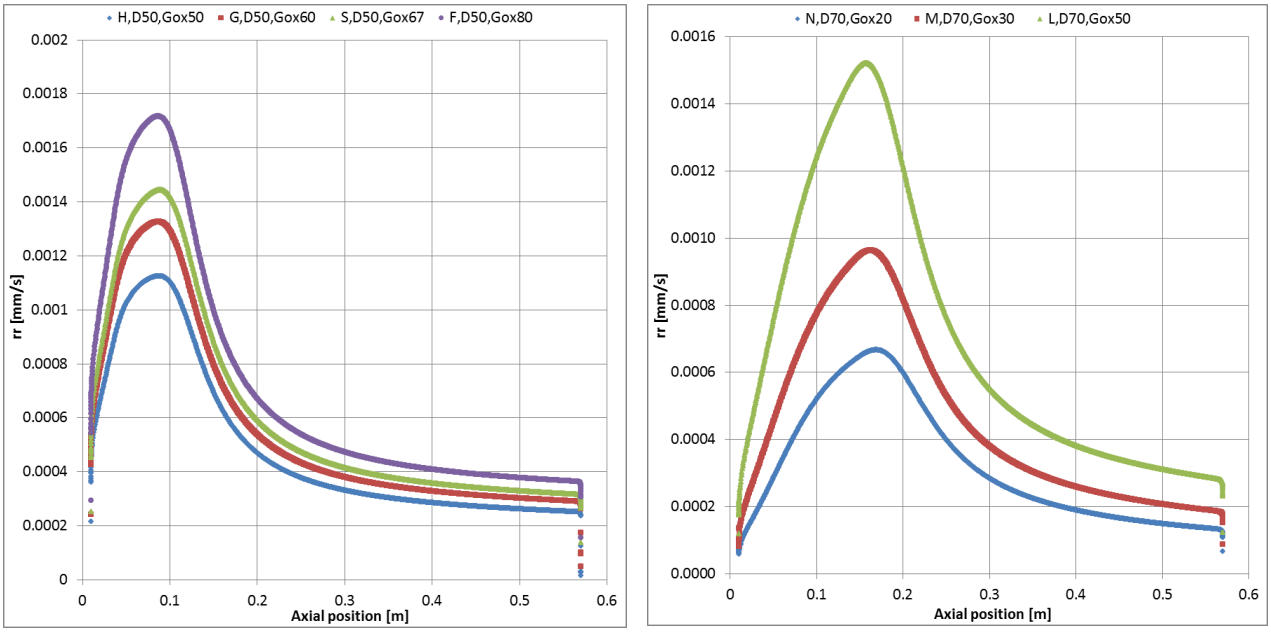

Figure 12: regression rate as a function of axial position along the fuel surface for two different port diameters, 50 mm (left) and 70 mm (right), and parametric for oxidizer mass flux

Finally fuel surface temperature has been compared case by case: the peak observed in correspondence of impingement spans from a minimum value of 980 K for case *S* to a maximum value of 1050 K for case K; the minimum level observed along the fuel surface is around 850 K.

These results highlight the role of the CFD simulations as a tool for the investigation of local details inside the hybrid motor combustion chamber.

7. Conclusions and Further Development

A numerical model of the ablation of classical polymeric fuels in hybrid rocket motors has been implemented on a commercial CFD code using a specific user-defined function that calculates regression rate, cell by cell, as a function of heat flux at the fuel surface. The regression rate is determined solving the energy balance at the surface coupled with the Arrhenius equation for fuel pyrolysis. A validation campaign has been successfully performed referring to literature data from a cylindrical port-axial injection lab-scale motor. The reference tests used the propellant combinations GOX-HTPB and GOX-HDPE where the gaseous oxygen was injected trough a single hole injector. The numerically determined fuel mass flows generally agree within 10% with the experimental results, thus proving the actual possibility to tailor a commercial software for the purpose and the effectiveness of a relatively simplified model in providing useful insight in the hybrid combustion process.

The CFD simulations allow the analysis of local phenomena inside the hybrid motor often difficult to study in detail. In fact, it has been shown that a significant local effect is present in the region where the oxidizer flow impinges on the fuel surface, enhancing the regression rate. The location and the intensity of this effect are determined by the diameter ratio between the port and the injection hole.

The proposed CFD tool can be used in order to investigate hybrid rocket regression rate behavior through parametric analysis, favoring the understanding of the ablation process and the definition of improved regression rate correlations. A future development of the current UDF could be the introduction of a suitable radiation model in order to increase the accuracy of the regression rate prediction, particularly for fuels that produce significant soot and/or at low oxidizer fluxes. Moreover, it will be useful to extend the model to non-classical fuels like for example liquefying fuels (with the addition of an entrainment model) or fuels with energetic additives (e.g. metal particles).

8. References

[1] Merkle, C. L. and Venkateswaran, S., 1996. Theoretical Investigation. In: *Fundamental Phenomena on Fuel Decomposition and Boundary-layer Combustion Processes with Applications to Hybrid Rocket Motors*, Part II. Propulsion Engineering Research Center, the Pennsylvania State University.

[2] Akyuzlu, K., Kagoo, R. and Antoniou, A., 2001. A Physics Based Mathematical Model to Predict Regression Rate in an Ablating Hybrid Rocket Solid Fuel. In: *37th AIAA Joint Propulsion Conference & Exhibit*, AIAA-2001-3242, Salt Lake City, UT.

[3] Serin, N., Gogus, Y. A., 2003. Navier-Stokes Investigation on Reacting Flow Field Of HTPB/O2 Hybrid Motor and Regression Rate Evaluation. In: *39th AIAA Joint Propulsion Conference & Exhibit*, AIAA-2003-4462, Huntsville, AL.

[4] Antoniou, A., Akyuzlu, K. M., 2005. A Physics Based Comprehensive Mathematical Model to Predict Motor Performance in Hybrid Rocket Propulsion System. In: *41th AIAA Joint Propulsion Conference & Exhibit*, AIAA-2005-3541, Tucson, AZ.

[5] Guobiao, C. and Hui, T., 2006. Numerical Simulation of the Operation Process of a Hybrid Rocket Motor. In: *42th AIAA Joint Propulsion Conference & Exhibit*, AIAA-2006-4506, Sacramento, CA.

[6] Bianchi, D., Urbano, A., Betti, B., and Nasuti, F., 2013. CFD Analysis of Hybrid Rocket Flowfields Including Fuel Pyrolysis and Nozzle Erosion. In: *49th AIAA Joint Propulsion Conference & Exhibit*, AIAA-2013-3637, San Jose, CA.

[7] Parissenti G., et al., 2011. Throttleable hybrid engine for planetary soft landing. In: *4th European Conference for Aeronautics and Space Sciences (EUCASS)*. St. Petersburg, Russia.

[8] Faenza, M., Moretto, F., Barato, F., Bettella, A. and Pavarin, D., 2013. Numerical and Experimental Activities in Support of the Development of Hybrid-Rocket Engines for Soft-Landing Applications. In: *5th European Conference for Aeronautics and Space Sciences (EUCASS)*. Munich, Germany.

[9] Kuo K. K. and Houim R. W., 2011. Theoretical Modeling and Numerical Simulation Challenges of Combustion Processes of Hybrid Rockets. In: *47th AIAA Joint Propulsion Conference & Exhibit*, AIAA-2011-5608, San Diego, CA.

[10] Chiaverini M., 2007. Review of Solid-Fuel Regression Rate Behavior in Classical and Nonclassical Hybrid Rocket Motors. In: *Fundamentals of Hybrid Rocket Combustion and Propulsion*, Progress in Astronautics and Aeronautics, vol. 218, 37-127.

[11] Lengellé, G., 1970. Thermal Degradation Kinetics and Surface Pyrolysis of Polymers. In: *AIAA Journal*, Vol. 8, No. 11, pp. 1989-1996.

[12] Lengellé, G., Fourest, B., Godon, J. C., Guin, C., 1993. Condensed Phase Behavior and Ablation Rate of Fuels for Hybrid Propulsion. AIAA Paper 93-2413.

[13] Lengellé G., 2007. Solid-Fuel Pyrolysis Phenomena and Regression Rate, Part 1: Mechanisms. In: *Fundamentals of Hybrid Rocket Combustion and Propulsion*, Progress in Astronautics and Aeronautics, vol. 218, 127-165.

[14] Carmicino C., 2002. Alcuni Aspetti della Balistica Interna di un Endoreattore a Propellenti Ibridi e del Comportamento di Ugelli a Spina Troncata. *PhD Thesis*, University of Naples "Federico II", Faculty of Engineering.

[15] Carmicino, C., Russo Sorge, A, 2005. Role of Injection in Hybrid Rockets Regression Rate. In: *Journal of Propulsion and Power*, Vol. 21, No. 4.

[16] Carmicino, C., Russo Sorge, A., 2006. Influence of a Conical Axial Injector on Hybrid Rocket Performance. In: *Journal of Propulsion and Power*, Vol. 22, No. 5.

[17] Carmicino, C., Orlandi, O., Russo Sorge, A., Dauch, F., De Amicis, R., De Rosa, M., 2006. Basic Aspects of the Hybrid Engine Operation. In: *45th AIAA Joint Propulsion Conference & Exhibit*, AIAA-2009-4937, Denver, CO.

[18] Carmicino, C., Russo Sorge, A., 2011. Advanced Solid Fuels for Hybrid Propulsion: the Research Activity in Europe. In: *47th AIAA/ASME/ASEE Joint Propulsion Conference & Exhibit*, AIAA-2011-5820, San Diego, CA.

[19] Kuo K. K., 2012. Solid Propellants and Their Combustion Characteristics. In: *Turbulent and Multiphase Combustion*, ch. 1, Wiley ed.

[20] Withmore, S. A., Peterson W. Z., Eilers, S. D., 2011. Analytical and Experimental Comparison of HTPB and ABS as Hybrid Rocket Fuels. In: *47th AIAA Joint Propulsion Conference & Exhibit*, AIAA-2011-5909, San Diego, CA.

[21] Kubota, N., 1984. Survey of Rocket Propellants and Their Combustion. In: *Fundamentals of Solid-Propellant Combustion*, Progress in Aeronautics and Astronautics, vol. 90, 38–40.

[22] Zilliac, G., Karabeyoglu, M. A., 2006. Hybrid Rocket Fuel Regression rate Data and Modeling. In: *42nd AIAA Joint Propulsion Conference & Exhibit*, AIAA-2006-4504, Sacramento, CA.

[23] NIST-JANAF thermochemical database.

[24] ICT database of thermochemical values.

[25] Purdue School of Aeronautics and Astronautics, Combustion and Thermochemical data.

[26] PROPEP database.

[27] De Wilde, J.P., 1988. The Heat of Gasification of PE and PMMA. Memorandum M-593, Delft University of Technology, Delft, The Netherlands.

[28] Stoliarov, S. I., Crowley, S., Lyon, R. E., Predicting the Burning Rates of Noncharring Polymers, Technical Report DOT/FAA/AR-TN09/16, U.S. Department of Transportation, Federal Aviation Administration, July 2009, Linwood, New Jersey.

[29] NASA-Glenn thermodynamic database.

[30] Personal communications between UPD researchers and Eng. Jan-Erik Ronningen from NAMMO Raufoss AS, in the framework of the SPARTAN Project.

[31] Faenza, M., Englaro, A., Lazzarin, M., Bettella, A., Pavarin D., 2013. Advanced CFD Investigation for Predicting Regression Rate in Hybrid Rockets. In: *49th AIAA Joint Propulsion Conference & Exhibit*, AIAA 2013-3898, San José, CA.